Inverse Approach to Spacecraft Charging Simulations

P. A. Resendiz Lira🆔, G. L. Delzanno, H. C. Godinez,
M. G. Henderson, B. Wohlberg🆔, *Fellow, IEEE*, and D. Svyatsky

Abstract—Spacecraft charging is a major topic of space-weather research since charging can lead to spacecraft anomalies, ranging from inconsequential to catastrophic. Spacecraft surface charging calculations use sophisticated numerical codes and are typically performed with a direct (forward) approach: the local properties of the space environment, the spacecraft geometry, and the spacecraft material properties are the input, while the electric field on and around the spacecraft and the corresponding plasma particle distributions are the output. This approach can be limited or highly inaccurate when some of the critical input parameters are either unknown or have large uncertainties. For instance, the Van Allen Probes spacecraft, also known as RBSP, is an example of a modern spacecraft with state-of-the-art measurements. Predicting the RBSP spacecraft potential requires knowledge of the cold and warm plasma populations which dominate surface charging. However, the cold plasma properties (particularly temperature) are not well characterized. In addition, the material properties are known from measurements in laboratory "clean" conditions but how materials age in space due to their interaction with the environment is not well understood. To mitigate these limitations, we developed an inverse approach to use available spacecraft-charging data to infer some of the unknown properties of the space environment around the spacecraft and spacecraft material degradation. Our inversion is composed of an ensemble of constrained optimization solutions that provide an estimate of the parameter values of interest. Our approach is validated with an analytical model of spacecraft charging, based on the orbital-motion-limited theory, together with a quasi-Newton optimization method. Our results show convergence and the ability to estimate the correct parameters in synthetic observation experiments.

Index Terms—Inverse problem, magnetospheric cold plasma, material aging in space, plasma diagnostics, spacecraft charging.

I. Introduction

SPACECRAFT orbiting the near-Earth environment acquire a net electric charge by collecting plasma particles from the ambient space plasma and by emitting electrons via secondary emission due to electron/ion impact or photo-emission on surfaces exposed to sunlight [1], [2]. Several plasma populations coexist in the near-Earth environment: the cold and dense particles of the plasmasphere (energy $\sim$electronvolt), the

warm plasma of the plasma sheet/ring current ($\sim$1–100 s keV) and the hot and rarefied radiation belts ($\sim$megaelectronvolt). These populations are responsible for different types of spacecraft charging. Cold and warm plasma particles deposit their charge on spacecraft surfaces and give rise to *surface charging*, while hot electrons can penetrate satellite shielding and reach internal components causing *deep-dielectric charging* [1], [2]. Surface charging can be nonuniform on the spacecraft, causing potential differences across adjacent surfaces (i.e., *differential charging*). Spacecraft charging is a critical topic in space-weather research since charging can lead to spacecraft anomalies [3], [4], [5], [6], [7]. The latter can range from inconsequential (e.g., single-event upsets and memory bit flipping) to catastrophic (damage to sensitive electronics or total loss of the spacecraft). Galaxy XV is a recent example of a spacecraft possibly lost due to surface charging after a geomagnetic storm [7].

Over several decades, sophisticated numerical tools have been developed to predict spacecraft surface charging. Such tools include community codes, for example, NASCAP [8], SPIS [9], MUSCAT [10], as well as research codes such as CPIC [11], [12], PTetra [13], and others. These tools are generally applied in a *direct* or *forward* approach, that is, the plasma environment, and the spacecraft geometry and materials are the inputs of the code. The output is then the electric field on and around the spacecraft, as well as the spacecraft potential, and the plasma particle distributions consistent with this electric field.

There are two major difficulties in accurately performing a direct spacecraft charging calculation. The first is that the parameters that characterize the magnetospheric cold plasma are typically unknown due to the difficulty of in situ measurements of the cold populations in the Earth's magnetosphere, as discussed in a recent review of the impact of the cold plasma in magnetospheric physics [14]. Second, materials can undergo significant changes once the spacecraft is in orbit, and hence their associated parameter values can have large uncertainties. Materials for space applications are well characterized in the laboratory before launch, but, once in orbit, these materials are exposed to the harsh space environment and their properties are strongly modified (see, e.g., [15] and [16]). Unfortunately, we do not yet have any robust methodology to assess and quantify material aging in space. Given the challenges of direct charging calculations in the Earth's magnetosphere, we propose an inverse charging calculation as a complement. The idea is to use the available spacecraft charging data (for

instance, the spacecraft potential or even direct information from the booms measuring the electric field near the spacecraft) together with other available environmental parameters as input to a spacecraft charging calculation to estimate those parameters that are unknown or have large uncertainties.

There are a number of spacecraft charging inversion approaches that have been exploited by several authors in the past. A common technique on space missions is to estimate the plasma density from spacecraft potential data using an inverse approach. Similarly, some authors have used available spacecraft datasets to compute the photoelectron current which includes material parameter estimates in some form. In a seminal work, Grard [17] estimated photoemission parameters in space by combining laboratory measurements of photoemission from various materials with the best available solar spectrum data collected in space. Pedersen et al. [18] determined a relation between spacecraft potential, space plasma density, and electron flux by using data from GEOS-1, GEOS-2, and ISEE-1. The photoelectron current density was also calculated using material parameters estimated by [17]. Schmidt and Pedersen [19] related the spacecraft potential of GEOS-2 with the background plasma density. Escoubet et al. [20] used the ISEE-1 spacecraft potential data to estimate the ambient electron density in the magnetosphere with high accuracy in time. In the first step, material parameters were estimated using a nonlinear least-square fit based on electron temperature, density, and spacecraft potential data from CDAW 6 and from the work of [19]. Once the photoemission parameters were known, the spacecraft potential was computed and fit that of the ISEE-1 spacecraft using the electron temperature and density as fitting parameters. Ishisaka et al. [21] estimated the electron density of the solar wind and the electron foreshock using the GEOTAIL spacecraft potential data. Nakagawa et al. [15], on the other hand, used the GEOTAIL spacecraft potential and electron density data to estimate material properties instead. It was found that material parameters in space have higher values compared to those predicted by [17] but were consistent with previous in-flight measurements from GEOS-, ISEE-1, and Viking. Scudder et al. [22] fit the photoelectron current density with two exponential functions using POLAR spacecraft data. Similarly, Thiebault et al. [23] fit the photoelectron current with a sum of two half-Maxwellians to determine the plasma density relation with the Cluster spacecraft potential data. On the other hand, Pedersen et al. [24] also estimated the electron density using the Cluster spacecraft potential data, but obtained the photoelectron current density using the CIS ion density and the WHISPER electron density measurements. Finally, Boardsen et al. [25] used the material parameters estimated by [22] to calculate the electron temperature of the inner low-density magnetospheric plasma using an inverse approach based on the POLAR spacecraft data. Although all the works described above used an inverse approach, to the best of our knowledge, ours is the first inverse-spacecraft charging technique that estimates both material parameters and some of the plasma parameters at the same time and this is the main contribution of our article.

The article is organized as follows: Section II presents the mathematical approach of our inverse technique. Section III presents the outcome and discussion of our inversion method using synthetic data experiments. Finally, in Section IV, we provide a summary of our findings and future work.

II. METHODOLOGY

To illustrate our inverse approach, we focus on what is perhaps the simplest charging regime, a positively charged, conducting spacecraft in sunlight immersed in the magnetospheric cold (∼electronvolt energy) plasma, where the spacecraft potential ϕ_{sc} is dictated by the emission of the photoelectrons balancing the collection of ambient cold electrons. The thermal ion current is negligible for these conditions, while secondary electron emission is not considered here. For simplicity, we will consider the ambient cold plasma represented by a Maxwellian phase space density.

The electron current collected by a conducting spherical spacecraft can be approximated using the orbital motion limited (OML) theory [26] as follows:

$$I_e = -e4\pi r_{sc}^2 n_e \sqrt{\frac{T_e}{2\pi m_e}} \exp\left(\frac{e\phi_{sc}}{T_e}\right), \quad \text{for} \quad \phi_{sc} < 0 \quad (1)$$

$$I_e = -e4\pi r_{sc}^2 n_e \sqrt{\frac{T_e}{2\pi m_e}} \left(1 + \frac{e\phi_{sc}}{T_e}\right), \quad \text{for} \quad \phi_{sc} \geq 0. \quad (2)$$

The photoelectron current, approximated with a single Maxwellian distribution [17], is given by the following equation:

$$I_{ph} = \mathcal{A}4\pi r_{sc}^2 J_{ph}, \quad \text{for} \quad \phi_{sc} < 0 \quad (3)$$

$$I_{ph} = \mathcal{A}4\pi r_{sc}^2 J_{ph}\left(1 + \frac{e\phi_{sc}}{T_{ph}}\right)\exp\left(-\frac{e\phi_{sc}}{T_{ph}}\right), \quad \text{for} \quad \phi_{sc} \geq 0. \quad (4)$$

Here, r_{sc} is the radius of the spacecraft, which is taken to be spherical, e is the positive elementary charge, and m_e, n_e, and T_e are the mass, density, and temperature of the ambient electrons, respectively. For photoelectron emission, T_{ph} and J_{ph} are the temperature and current density of the photoelectrons, respectively, while $\mathcal{A}$ is the fraction of the spacecraft illuminated area relative to the total surface area. The spacecraft surface charging is then computed by solving the equilibrium equation (i.e., floating condition)

$$I_e(\phi_{sc}, n_e, T_e) + I_{ph}(\phi_{sc}, T_{ph}, J_{ph}) = 0. \quad (5)$$

Note that OML can be a poor approximation to the transition between negatively and positively charged regimes [27] but we shall not be concerned about that here since the objective is to demonstrate the technique in a simple charging model. Let us now specialize in the application of the inverse charging technique to spacecraft data available from in situ measurements. As a reference, we use the NASA Van Allen Probes spacecraft, also known as RBSP, a modern spacecraft with state-of-the-art measurements that operated between 2012 and 2019 to study the dynamics of the Earth's radiation belts. The measurements available from RBSP include the spacecraft potential, the total electron density, and fluxes of electron populations with

energies larger than 15 eV. The spacecraft geometry is also known. The spacecraft potential, the density of the cold electrons (inferred from the total electron density), and the geometry of the spacecraft are inputs to the inverse calculation. The temperature of the cold electrons and the photoemission parameters will then be the output of the inverse technique. Note that we assume that photoemission is dominated by the RBSP solar panels coated with ITOC (since, nominally, this is much higher than that from the black Kapton body [28] so that photoemission can be characterized by only one spacecraft material). Furthermore, for most of the synthetic experiments presented in Section III, we only consider a single Maxwellian component for the photoelectrons. However, it is known from past spacecraft missions that photoelectron emission can be approximated by a sum of multiple Maxwellian components with different energies and current densities [15], [22]. The use of a single Maxwellian component here is justified by the fact that by we are targeting a relatively narrow range of low spacecraft potential values, 0–10 V in our experiments, where the contribution of the additional Maxwellian components to the photoelectron current is less important and can be neglected. Nakagawa et al. [15] show that at lower values of spacecraft potential (a few V), the photoelectron current is dominated by the contribution of the Maxwellian with the lower temperature and higher current density. Meanwhile, at higher values of the spacecraft potential, the current is dominated by the Maxwellian with the higher temperature but lower current density value. Sensitivity of the inverse technique to this assumption is assessed in Section III-F. Finally, we note that, because of the spacecraft's motion, the plasma parameters can change very quickly, on time scales of seconds. The material parameters, on the other hand, are expected to change on longer time scales (weeks to months) and therefore can be considered constant if we use spacecraft data in hours/days periods.

Our inverse charging technique will take $\phi_{sc}(t)$, $n_e(t)$, and the spacecraft geometry as inputs such that, through (5), we can write symbolically

$$\phi_{sc}(t) = \phi_{sc}(T_e(t), T_{ph}, J_{ph}) \tag{6}$$

with t time. The output of the technique is then $T_e(t)$, T_{ph}, and J_{ph}.

Our technique utilizes a constrained minimization approach to estimate the output parameters such that the appropriate values of the parameters of interest are given by the following equation:

$$T_e(t), T_{ph}, J_{ph} = \underset{T_e(t), T_{ph}, J_{ph}}{\operatorname{argmin}} \left\| \phi_{sc}(T_e(t), T_{ph}, J_{ph}) - \phi_{sc}^{obs} \right\|$$
$$\text{subject to}: I_e(\phi_{sc}(t), n_e(t), T_e(t))$$
$$+ I_{ph}(\phi_{sc}(t), T_{ph}, J_{ph}) = 0 \tag{7}$$

where $\phi_{sc}(t)$ is the surface charging estimation provided by OML, while $\phi_{sc}^{obs}(t)$ is the observed surface charging data available for instance from RBSP, and $\|\cdot\|_2$ is the L^2 - norm.

As stated above, the problem is under-determined. If we have N observations of the spacecraft potential at different times, we need to estimate $N + 2$ unknowns: N points in time corresponding to T_e, and the two material parameters
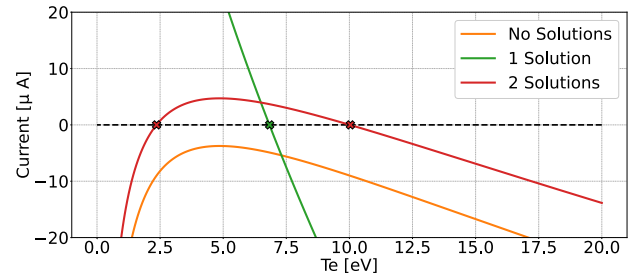

Fig. 1. Possible solutions for the electron temperature given all other parameters as in Table I. T_e solutions are given where the colored lines cross $I = 0$ (black dashed line). In this example, there are zero, one, and two solutions for T_e represented by the crossing at $I = 0$ of the orange, red, and green lines, respectively.

that are constant, T_{ph} and J_{ph}. To solve this issue, we use an expansion of T_e as a function of time using polynomials (or splines) as follows:

$$T_e = \alpha_0 + \alpha_1 t + \alpha_2 t^2 + \cdots = \sum_{k=0}^{N_T - 1} \alpha_k t^k \tag{8}$$

where α_k are the N_T coefficients of the polynomial to be determined. Assuming that $N \gg N_T + 2$, the minimization problem is reformulated as follows:

$$\alpha_k, T_{ph}, J_{ph} = \underset{\alpha_k, T_{ph}, J_{ph}}{\operatorname{argmin}} \left\| \phi_{sc}(\alpha_k, T_{ph}, J_{ph}) - \phi_{sc}^{obs} \right\|$$
$$\text{subject to}: I_e(\phi_{sc}(t), n_e(t), \alpha_k)$$
$$+ I_{ph}(\phi_{sc}(t), T_{ph}, J_{ph}) = 0 \tag{9}$$

which is now an overdetermined problem that can be solved in a least-squares sense.

The minimization problem, as stated in (9), is solved using a trust-region method [29] with appropriate constraints for the parameters J_{ph}, T_{ph}, and the coefficients α_k.

A. Possibility of Multiple Solutions for the Electron Temperature in the Inverse Technique

By inspecting (2) for $\phi_{sc} > 0$, it can be seen that the electron current depends on both $(T_e)^{1/2}$ and T_e, leading to a quadratic equation for $(T_e)^{1/2}$ when all the other parameters are given. This means that it is possible that two different values of the electron temperature exist for the same (positive) value of the spacecraft potential, considering all other parameters are fixed. Fig. 1 shows an example where different system parameters lead to a different number of possible solutions for the electron temperature T_e given the spacecraft potential. In the figure, the net current $I = I_e + I_{ph}$ is plotted as a function of T_e. The net current I is computed from (1) to (4) using the parameter values in Table I. The colored lines in the plot correspond to the results of using the different sets of parameters in the table. The number of solutions for T_e is given by the number of times that the colored lines cross $I = 0$ (black dashed line). The orange line never crosses $I = 0$, hence, there is no solution for T_e for the given parameters. The green line crosses $I = 0$ at $T_e = 6.84$ eV, thus, for the specified parameters, there is a unique solution for the electron

TABLE I
REFERENCE VALUES USED TO GENERATE THE I VERSUS T_e CURVES
SHOWN IN FIG. 1. THE TOTAL CURRENT I IS COMPUTED
AS $I = I_e + I_{ph}$ USING (1)–(4)

parameter	0 Solutions	1 Solution	2 Solutions	Units
n_e	53.6	175.6	48.0	$[cm^{-3}]$
ϕ_{sc}	4.86	-0.16	4.86	[V]
$\mathcal{A}$	0.5	0.3	0.5	
T_{ph}	2.0	2.0	2.0	[eV]
J_{ph}	40.0	40.0	40.0	$[\mu A/m^2]$

temperature. The red line crosses $I = 0$ at $T_e = 2.36$ eV and $T_e = 10.04$ eV. As such, for this set of parameters, two solutions for the electron temperature exist.

It must be noticed that the presence of two solutions for the electron temperature associated with the same spacecraft potential is not a numerical artifact: these are true physical solutions of the system. Although we have used an approximated, the semianalytical model (OML) for spacecraft charging, this feature has been confirmed with kinetic simulations (not shown) where the spacecraft potential is calculated with the first-principles model CPIC [11], [12]. Note that the possibility of multiple solutions for the electron temperature has been previously observed in the work done by [25]. Nevertheless, since these potential two solutions for T_e are physical, our inverse technique will be capable of finding them when they exist. This is also illustrated in an example shown in Section III-D.

III. RESULTS

The technique has been tested with synthetic experiments in which we specify the time-dependent profiles for density $n_e(t)$ and temperature $T_e(t)$ of the cold electrons as well as the photoemission material parameters T_{ph} and J_{ph} and compute the spacecraft surface potential using OML. We then feed the OML spacecraft potential $\phi_{sc}(t)$ and the cold electron density $n_e(t)$ to the inverse technique and use it to compute the cold electron temperature $T_e(t)$ and the photoemission parameters T_{ph} and J_{ph}. The computed values are compared against the reference values to evaluate the accuracy of the inverse technique.

We use some of the individual synthetic experiments to illustrate the inverse technique and some of the obstacles that needed to be overcome. For simplicity, in Sections III-A–III-C, we use an example case where only one solution for the electron temperature exits at each local time. On the other hand, in Section III-D, we show an example with two T_e solutions at each local time. To assess the accuracy of the technique, we report in Section III-E, the errors in the parameter estimation evaluated against 32 synthetic experiments independent of the ones used in Sections III-A–III-D. Last, in Section III-F, we showcase an example where the photoemission properties of the material are represented by two Maxwellians.

Note that time-dependent profiles of density and temperature of the plasma, the static photoelectron emission parameters, and the time-dependent profile of the estimated spacecraft potential for all the 36 cases considered in this study
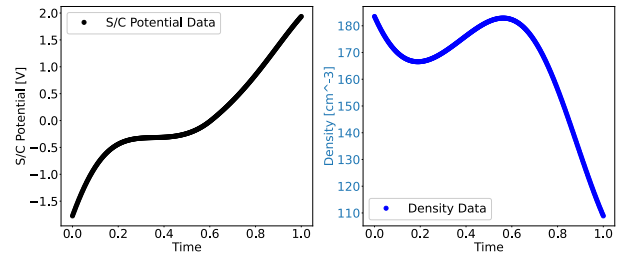

Fig. 2. Input to the inverse approach. Noise-free signal of spacecraft potential (left) and density (right) as a function of time.
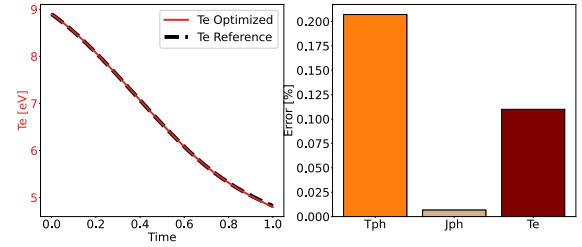

Fig. 3. Output of the optimization using noise-free input signals. Estimate of the electron temperature (left) and relative errors for material parameters and RMSE for $T_e(t)$ (right).

are stored in [30] with open access. For the 35 single material cases, we have used $T_{ph} = 2$ eV and $J_{ph} = 40$ μA/m^2 as nominal material parameters. Last, in all cases presented in this article, the spacecraft is approximated as a perfectly conductive sphere of radius 1 m.

A. Case I: Without Noise in the Observations Used as Input

First, we considered noise-free input signals for the density and spacecraft potential as a function of time. Fig. 2 shows an example of input data for the optimization. Fig. 3 shows the output of the inverse technique, that is, the electron temperature as a function of time (left) and the errors on the estimated parameters (right). We report relative errors for the material parameters: 0.2% and 0.007% for T_{ph} and J_{ph}, respectively. As for the error in the estimation of $T_e(t)$, we report the root-mean-squared-error (RMSE) which gives a better sense of the global error due to the time dependence of the electron temperature compared to, for instance, the maximum of the error over the whole time interval. In this example, the RMSE for $T_e(t)$ is 0.11%. Since very similar results were obtained for other examples which are not shown here, we conclude that, when the input data is free of noise, the technique allows parameters estimation with high accuracy [Fig. 3 (right)].

B. Case II: With Noise Added to the Observation Used as Input

In practical situations, in situ measurements have noise. Therefore, white noise was added to the spacecraft potential and to the cold electron density signals of the example in Section III-A to test the robustness of our inverse technique against noise. Fig. 4 shows an example of the spacecraft potential with 7% of white noise added (black dots). Since the technique performs exceptionally well with noise-free signals
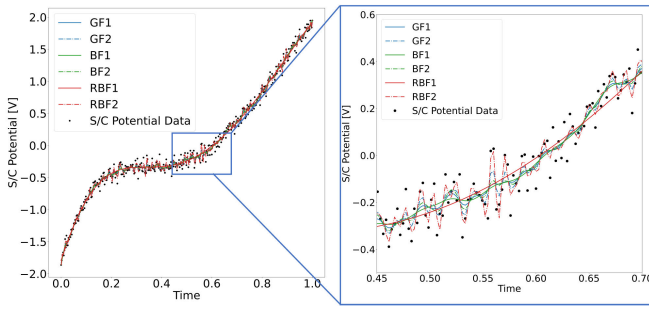
Fig. 4. Noisy signal of the spacecraft potential (black dots) smoothed using (GF, blue), (BF, green), and GPR with the RBF kernel (RBF, red) techniques.
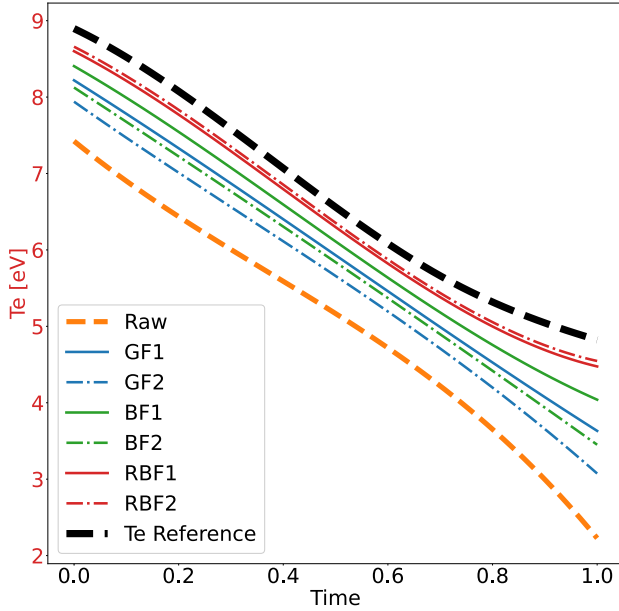

Fig. 5. Electron temperature solutions obtained with the inverse technique after smoothing the noisy input data in Fig. 4 using different techniques while varying parameters in the smoothing filters.

TABLE II
PARAMETERS USED IN THE SMOOTHING TECHNIQUES

| Gaussian Filter		
Parameter	Case 1	Case 2
sigma	2	0.85
order	0	0
output	None	None
mode	reflect	nearest
cval	0.0	0.0
truncate	4.0	7.0
Butter-worth Filter		
Parameter	Case 1	Case 2
f order	3	2
cutoff	0.127	0.257
output	'ba'	'ba'
Gaussian Process Regressor		
Parameter	Case 1	Case 2
GPR Kernel	RBF	RBF
length scale	1.0	1.0
length scale bounds	[1E-2, 1E3]	[1E-2, 1E3]
noise level	1E-1	1E-1
noise scale bounds	[1E-6,3E-3]	[1E-6,5E-5]
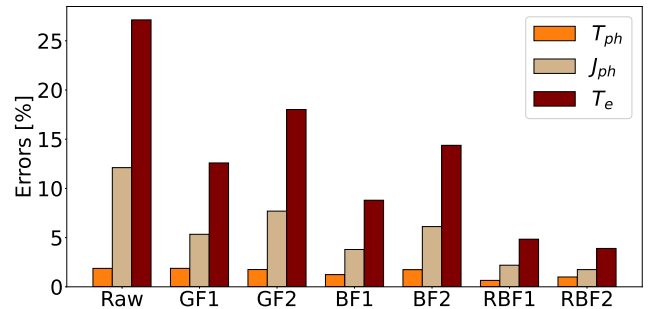
Fig. 6. Errors in the parameter estimation obtained after smoothing the noisy data in Fig. 4 using different techniques while varying parameters in the smoothing filters. Relative errors are given for the material parameters, T_{ph} and J_{ph}, while RMSE is for $T_e(t)$.

as input, the first obvious approach to deal with noise was to smooth the noisy observations using different filters with various filter parameters. Colored lines in Fig. 4 represent examples of smoothing the noisy spacecraft potential data (black dots) using the Gaussian filter (GF), Butterworth filter (BF), and Gaussian process regressor (GPR) with the radial basis function kernel (RBF) techniques. Then, the inverse procedure is applied on the smoothed data and the results are presented in Fig. 5, which shows the estimation of the electron temperature as a function of time.

Note that the colored curves shown in Fig. 5 correspond to the data-smoothing technique used with the parameters given in Table II. These filters are available in Python 3 from the scipy (scipy.signal) and Scikit-learn [31] libraries and the parameters listed in Table II are those that enable the application of those filters. For instance, the blue solid and dash-dotted lines labeled as "GF1" and "GF2" represent the use of the Gaussian filter for the parameters corresponding to cases 1 and 2 in Table II. Likewise, green and red curves correspond to the BF and GPR (using the RBF kernel), respectively. For reference, the inverse technique was also applied using the noisy data, that is, without smoothing it, and

the estimated $T_e(t)$ is labeled as "Raw" (orange dashed line) in Fig. 5. The filter parameters in Table II were chosen to vary the level of "smoothness" of the noisy signals used as inputs in the inverse technique and to assess its effect on the solution. In Fig. 4 (right), it can be seen that some combinations of filter parameters yield smoother curves (see, e.g., RBF1) compared to others that produce a more oscillatory representation of the noisy data (see e.g., RBF2).

The electron temperature as a function of time estimated by the inverse technique using the smoothed signals (Fig. 4) as inputs is shown in Fig. 5. Fig. 6 shows the errors in the estimated parameters corresponding to each one of the smoothing techniques in the same format as in Section III-A. Based on the results presented in Section III-A, we expected that the smoother curves would yield more accurate estimates of the parameters than what was found in practice. In fact, the lowest error in this example case is obtained when the least smoothed curve is used as input, that is, RBF2. The errors reported in Fig. 6 suggest that the RBF smoothing techniques yield the lowest errors, RMSE for T_e are RBF1 = 4.8% and RBF2 = 3.9%. Note, however, that RBF1 and RBF2 correspond, respectively, to the smoothest and least smooth curves, as can be seen in Fig. 4 (right). All other combinations of filter and parameters generated curves of the
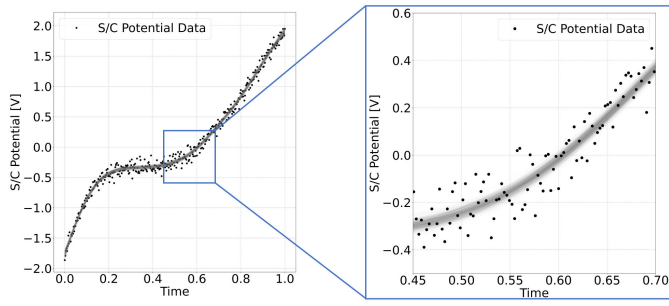
Fig. 7. Ensemble of inputs (gray lines) generated from the noisy input data (black dots) using the GPR technique.

input data with a smoothness degree intermediate between those obtained with RBF1 and RBF2. The fact that the least smooth curve yields the most accurate estimates, that is, RBF2, might suggest that the smoothing of the noisy data is unnecessary. However, when the noisy data was used as input without any smoothing (labeled as RAW in Figs. 5 and 6), the RMSE in the electron temperature was estimated at 27% and it is the largest error found in this example case. The most striking finding in this part of the study was that when the same filter parameters listed in Table II were applied to different synthetic examples, the results were not consistent with the ones presented in this example, that is, other filtering techniques produced the lowest errors. As a result, we were unable to find a robust approach to smooth the noise in the observations that would lead consistently to highly accurate estimation of the parameters. These results led us to conclude that the technique is very sensitive to noise in the input data.

C. Case III: Statistical Approach to Overcome Noise

To overcome the negative impact of noise in the observations, instead of using a deterministic approach, we resorted to a probabilistic approach. The idea is to create an ensemble of input functions representing the noisy input data, whose probability distribution respects the mean and the variance of the original data. For this part, we use the GPR with the RBF kernel [32]. With M functions of the input probability distribution, we solve M optimization problems and construct an ensemble of M solutions of the inverse technique and the related probability distributions for the output parameters. We found that taking the mean of the probability distribution of the solution ensemble allows one to statistically recover the parameter solution accurately. Fig. 7 shows an example of the ensemble of inputs generated with GPR. Using the mean and the variance of the input data, GPR calculates the probability distribution over all admissible functions that fit the data.

Fig. 8 shows the solution ensemble of the electron temperature as a function of time (gray lines). The red line (with red dots) is the solution computed as the mean of the solution ensemble at each local time. Examples of the probability distribution at three different local times are shown in the bottom row of Fig. 8. Here, one can appreciate that the probability distributions of the electron temperature at time = 0.24, 0.62, and 0.97 shown in Fig. 8 exhibit a single maximum. As such, we determined empirically that when the distribution at a given local time has a single maximum and the probability distribution locally approaches a normal distribution, the mean
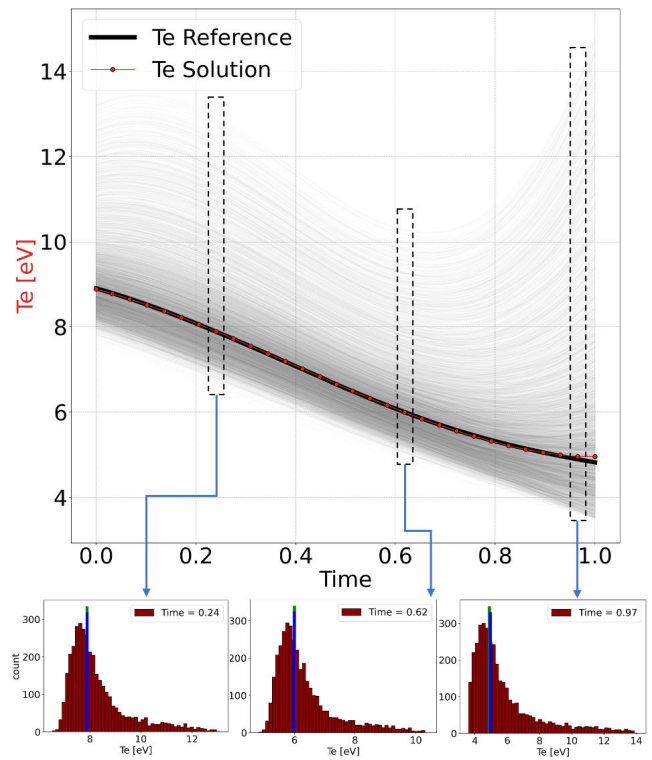

Fig. 8. Solution ensemble for the electron temperature (top). The probability distribution at selected local times (bottom) follows a quasi-normal distribution that allows the calculation of the electron temperature as a function of time (red line) by taking the mean of each of these distributions (black dots).

of the distribution is a good estimate of the parameter solution. Note that it is possible that at some local times, two solutions for T_e exist very close to each other. In these cases, the nature of this statistical approach will be to merge them into a single peak, with the local distribution possibly showing more departure from a normal distribution than in the example of Fig. 8. In such cases, the mean of the distribution is still a good estimate of the solution.

By applying this criterion, we were able to estimate $T_e(t)$ with high accuracy for the example case shown in Fig 8, where the reference solution for the electron temperature (black line) and the solution constructed by taking the mean of the probability distribution at each local time are extremely close to each other. Indeed, in this example, the RMSE for the cold electron temperature is only 0.48%. For completeness, the probability distributions of the material parameters are shown in Fig. 9. Since the material parameters are assumed to be constant over the time period considered, the final solution is computed as the mean of each distribution and is represented by the blue vertical lines in Fig. 9, while the true value of the material parameters is represented by the green lines. The relative errors for both material parameters, T_{ph} and J_{ph}, are 2.1% and 0.59%, respectively.

D. Case IV: Two Solutions for the Electron Temperature

A synthetic case with a single solution for T_e at each local time has been used in Sections III-A–III-C to showcase the steps and reasoning that led us to a statistical approach to estimate the output parameters of the inverse technique. In this
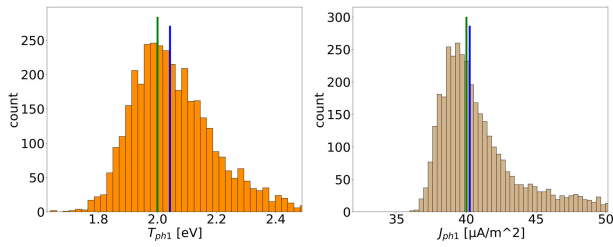
Fig. 9. Material parameters solution ensemble. The probability distribution for the temperature (T_{ph}) and current density (J_{ph}) of photoelectrons are shown on the left and right, respectively. Both ensembles show distributions that are reasonably approximated by a normal distribution. The final solution for both material parameters is computed as the mean of the distributions (blue vertical line), while the green vertical line represents the true solution.
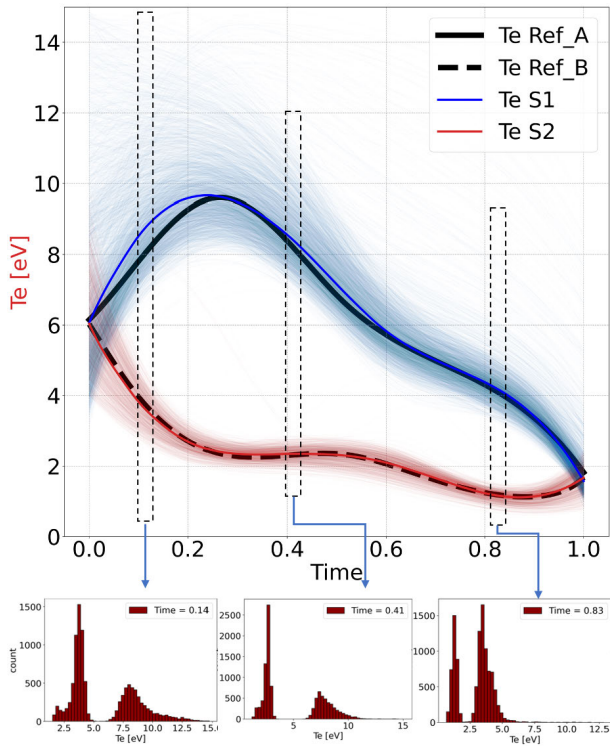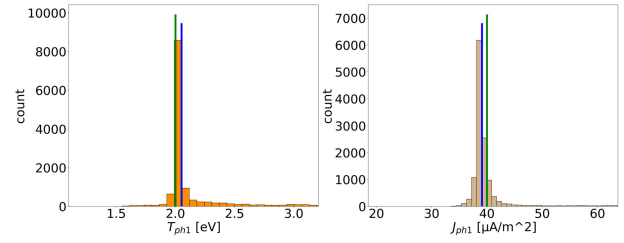

Fig. 11. Material parameters solution ensemble corresponding to the two solution example case. The probability distribution for the temperature (T_{ph}) and current density (J_{ph}) of photoelectrons are shown on the left and right, respectively. Despite the two solutions for the electron temperature, here both ensembles show normal distribution with a single maxima.

Fig. 10. Example of a case with two solutions in the electron temperature as a function of time $T_e(t)$. The red and blue dotted lines represent the two solutions found by our inverse technique for $T_e(t)$. The faded-thin red and blue lines represent the solution ensemble of the corresponding solution. The black solid and dashed lines are the true parameter values. In the bottom row, distributions at specified local times are shown. RMSE1 = 4.0% and RMSE2 = 2.27%.

section, we present a synthetic case where two solutions for the electron temperature exits at every point in time and can be clearly identified. The inputs and parameter solutions can be found in [30] under the *Case two T_e solution* folder. The T_e solution ensemble of this example case is shown in Fig. 10 (top) while examples of distributions at different local times are shown in the bottom. The thin-faded blue and red lines in the top of the figure represent the probability distribution of the corresponding T_e solution while the solid blue and red lines are the mean of such distributions, that is, the final solutions. The solid and dashed black lines represent the two true solutions for T_e.

By examining the T_e distributions at local time = 0.14, 0.41, and 0.83 in the bottom of Fig. 10, the two solutions can be

easily identified by the two peaks in the distributions. This example shows that our inverse charging technique is capable of finding the two possible solutions of T_e very accurately. The RMSE, estimated with respect to the corresponding reference solution (solid and dashed black lines), is 4.0% for solution one (blue) and 2.27% for the second solution (red). We conclude that the inverse technique can estimate both physical solutions accurately.

Regarding the estimation of the material parameters for this example, their solution ensembles are shown in Fig. 11 where only a single peak is present in both distributions. The single peak in both probability distributions confirms that the two different values found for T_e are true physical solutions of the system having all other parameters fixed (n, ϕ_{sc}, T_{ph} J_{ph}, and $\mathcal{A}$). Moreover, despite the two solutions for T_e in this example, the technique can estimate the material parameters very accurately: the relative errors for T_{ph} and J_{ph} are 2.6% and 2.3%, respectively.

We note that, in practical cases, the fact that there might be two physical solutions for T_e could result in large errors in the estimation of the parameters if one is unable to determine which one is the desired solution. In such cases, the relative error would become the order of the difference between the two solutions, which for the example of Fig. 10 could be more than 100%. In practice, however, one might be able to choose the right solution based on physics considerations, such as, for instance, by using data from a particle instrument to identify whether the particle distributions match one of the two temperature solutions or not. Another option, for cases where the two solutions might occur only in part of the time domain, could be to track the one solution that covers the whole time domain. Another thing to consider is that there could be cases where two (or more) different sets of parameters, including different material parameters, could fit the same input spacecraft potential. This would show as two peaks in the probability distributions of the estimated parameters. Assuming that material parameters do not change on time scales of hours to days, one might be able to discard one of the two sets of solutions by comparing adjacent time intervals.

E. Results of 32 Synthetic Experiments

To test its robustness, we applied the inverse statistical approach to 32 new synthetic cases, where the density and temperature (as a function of time) were varied in a specific range of parameters. The profiles of the density and tempera-

ture of the cold electrons, material parameters, and spacecraft potential for all synthetic cases can be found in [30]. Note that in the example presented in Section III-C, only one solution of T_e was found at each local time, while the example presented in Section III-D had two solutions. In practice, one or two solutions of T_e could be found at any given local time along the entire time interval. Thus, if the probability distribution at a given local time resembles a normal-type distribution with a single maximum, we compute a single T_e solution as the mean of the distribution (as done in Section III-C). If two solutions are clearly identified in the ensemble solution at a given local time, that is, the distribution shows two clearly identifiable and well-separated peaks, we compute two solutions by taking the mean of each distribution independently (as done in Section III-D). Similar to what was shown in Section III-D, for those local times where the technique finds two solutions for T_e, it is possible to compute two RMSE errors as well. This allows us to assess the accuracy of our approach independent of the number of solutions found for T_e. On the other hand, if the distribution at a given time does not resemble locally a normal-type distribution, the calculation of the solution is discarded and not accounted for in the final solution of the electron temperature as a function of time. This means that, in practical cases, it might not always be possible to estimate T_e accurately at each point of the time interval, as it was done for the cases in Sections III-C and III-D. Nonetheless, across all 32 cases considered here, those local times on which no-acceptable solutions were found correspond, on average, to less than 20% of the entire time interval. Last, since we are interested in computing the temperature of the cold electrons whose values are of the order of several eV in the examples considered ($T_e < 11$ eV in all cases), we have imposed a 15 eV cutoff in the technique, that is, we automatically discard any solution with $T_e > 15$ eV.

Fig. 12 shows the errors in the parameter estimation for the 32 cases. The first and second rows show the relative errors for the material parameters, T_{ph} and J_{ph}, respectively. The estimation of the photoemission parameters is extremely accurate with no more than 6% error across all cases considered. As for the electron temperature, two RMSE estimates are given as explained above. The first RMSE is shown in the third row while the second RMSE is in the fourth row. Both RMSE values remain below 15% across all cases. Note that it was only possible to compute the second RMSE value in six out of 32 cases. This is because: 1) not all 32 cases have two solutions along the time interval and 2) when two T_e solutions are present at a given local time, it is sometimes difficult to separate clearly both solutions (contrary to what it was shown in the example in Section III-D) and thus, the computation of the solution is discarded under such circumstances. Overall, the methodology presented here allows us to overcome the noise in the input data to recover the parameters robustly and with high accuracy.

F. Inversion Technique With Photoemission From Two Distinct Materials

In all synthetic experimental results presented so far, including those in Section III-E, it is assumed that photoelectrons
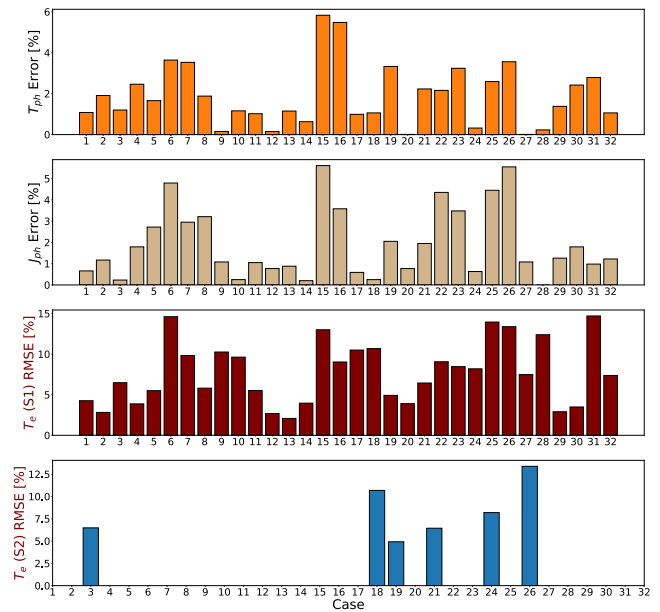

Fig. 12. Computed errors of the parameters estimated by the inverse technique applied to 32 synthetic cases. The relative error is shown for the material parameters in the first and second rows. For the electron temperature, the root-mean-square error is reported in the third and fourth rows.

are emitted from a single surface material according to a Maxwellian distribution characterized by a single temperature. This assumption was in part motivated by the fact that we are targeting the RBSP spacecraft as a case of study. RBSP is a Sun-pointing spacecraft where a portion of the illuminated area is covered with a low photoemitting material [black Kapton, $J_{ph} = 2$ μA/m^2, NASA material, and processes technical information system (MAPTIS)], whereas the solar panels are covered with a higher photoemitting material (ITOC, $J_{ph} = 16.8$ μA/m^2, and NASA MAPTIS). Moreover, the illuminated area $\mathcal{A}$ covered with ITOC is more than twice the one covered with Kapton. Thus, in this case, we expect photoemission to be dominated by the material with the higher J_{ph} and larger $\mathcal{A}$. Aditionally, we considered fairly low values of S/C potential so that photoemission could be represented by a single Maxwellian. Since, in general, design and materials can vary considerably from spacecraft to spacecraft, it is of interest to understand whether the inversion technique can recover accurately cases where photoemission occurs from different materials. We address this question here for a case with two distinct photoemitting materials contributing to the overall current balance. Note that the two materials case treated here is formally equivalent to having a single material emitting photoelectrons at two different energy bands, as suggested in [15] and [22].

An example of a case where two materials significantly contribute to spacecraft charging is shown in Fig. 13, where the photoelectron current is plotted as a function of the spacecraft potential. In this example, the parameters of the first material are $T_{ph1} = 2$ eV, $J_{ph1} = 80$ μA/m^2, and $\mathcal{A} = 0.3$, while for the second material, we have $T_{ph2} = 10$ eV, $J_{ph2} = 30$ μA/m^2, and $\mathcal{A} = 0.3$. In Fig. 13, one can clearly see that the first material (orange line) contributes more to the current balance at lower
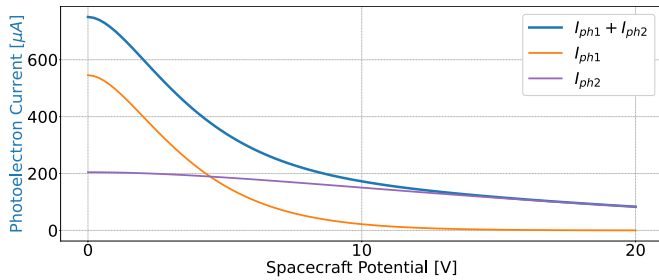
Fig. 13. Photoelectron current given by the contribution of two materials with different photoemission properties. The orange line represents the current of the first material, whereas the purple line is the contribution from the second one. The total current is represented by the blue line.
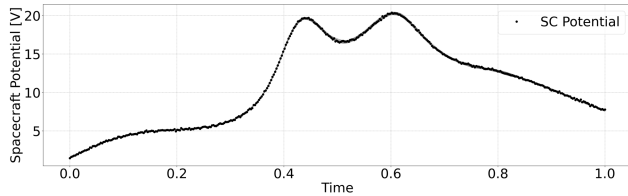

Fig. 14. Spacecraft potential as a function of time used in the example where photoemission from two materials contributes to the current balance.
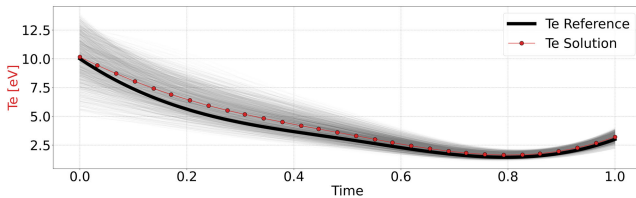

Fig. 15. Solution ensemble of the electron temperature as a function of time. $T_e(t)$ is recovered accurately even when two materials contribute to the photoelectron current. The red line represents the solution computed by the inverse technique, whereas the black one is the true solution.
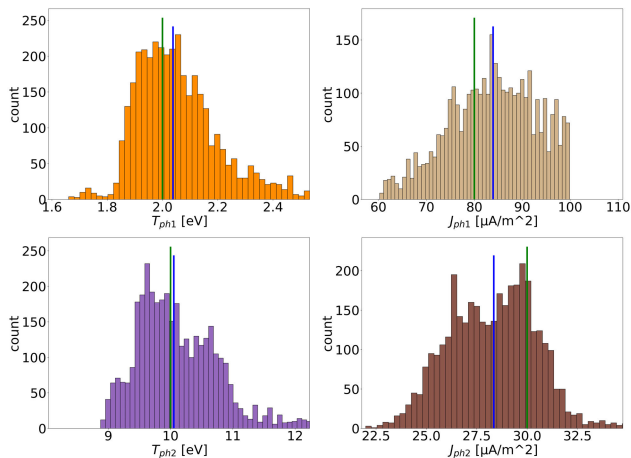

Fig. 16. Material parameters solution ensemble. The probability distribution for the temperature and current density of the photoelectrons for the first and second materials are shown in the top and bottom rows, respectively. As in the case of a single material, the final solution is computed as the mean of each distribution.

spacecraft potential values, whereas the second one (purple line) dominates at higher values of the spacecraft potential. The total current from both materials is represented by the blue line in Fig. 13.

By looking at Fig. 13, it is expected that if the spacecraft potential given as input to the inverse technique covers the range where each of the two materials can contribute significantly to the current balance, our inverse technique should be able to estimate accurately the parameters of the two materials as well as the electron temperature as a function of time. Figs. 15 and 16 show $T_e(t)$ and the material parameters solution ensembles for an example case where the two materials, with the photoemission parameters as in Fig. 13, were considered. The spacecraft potential used as input in the inverse technique, in this case, is shown in Fig. 14. As can be seen in Figs. 15 and 16, the technique estimates the parameters with high accuracy: the RMSE for T_e is 13.57%, while the relative errors in T_{ph1} and J_{ph1} for the first material are 2% and 5%, respectively. For the second material, the relative errors in T_{ph2} and J_{ph2} are 0.5% and 5.5%, respectively.

IV. CONCLUSION

We developed an inverse spacecraft surface charging technique that, for the first time, can estimate spacecraft material parameters and some properties of the ambient plasma simultaneously. The inverse technique is based on a statistical approach to overcome issues associated with noise in the input data. In this work, we have explored its application to a specific charging regime where a conducting spacecraft is positively charged in sunlight due to the balance between photoemission and the collection of cold electrons. Several synthetic experiments showed that the inverse technique could recover the output parameters robustly and with high accuracy.

Despite the proof-of-principle nature of this study, once mature, this technique could have important scientific and practical applications. It enables a method to obtain some of the properties of the environment (i.e., the cold plasma populations) that are typically very hard to obtain. This is of particular interest to the magnetospheric cold-plasma community and it supports work toward new cold-plasma space missions that are being pursued. Another key aspect is that it delivers a new way to study material aging in space. Finally, this technique can aid spacecraft anomaly resolution, since it gives the spacecraft a "material identification card" which is a necessary ingredient in any forensic work to attribute anomalies to the space environment.

ACKNOWLEDGMENT

REFERENCES

[1] D. Hastings and H. Garrett, *Spacecraft-Environment Interactions*. Cambridge, U.K.: Cambridge Univ. Press, 2004.

[2] S. Lai, *Fundamentals of Spacecraft Charging*. Princeton, NJ, USA: Princeton Univ. Press, 2011.

[3] D. N. Baker, "The occurrence of operational anomalies in spacecraft and their relationship to space weather," *IEEE Trans. Plasma Sci.*, vol. 28, no. 6, pp. 2007–2016, Dec. 2000.

[4] D. N. Baker, "How to cope with space weather," *Science*, vol. 297, no. 5586, pp. 1486–1487, Aug. 2002.

[5] H.-S. Choi et al., "Analysis of GEO spacecraft anomalies: Space weather relationships," *Space Weather*, vol. 9, no. 6, Jun. 2011, Art. no. S06001.

[6] M. F. Thomsen, M. G. Henderson, and V. K. Jordanova, "Statistical properties of the surface-charging environment at geosynchronous orbit," *Space Weather*, vol. 11, no. 5, pp. 237–244, May 2013.

[7] D. C. Ferguson, S. P. Worden, and D. E. Hastings, "The space weather threat to situational awareness, communications, and positioning systems," *IEEE Trans. Plasma Sci.*, vol. 43, no. 9, pp. 3086–3098, Sep. 2015.

[8] M. J. Mandell, V. A. Davis, D. L. Cooke, A. T. Wheelock, and C. J. Roth, "Nascap-2k spacecraft charging code overview," *IEEE Trans. Plasma Sci.*, vol. 34, no. 5, pp. 2084–2093, Oct. 2006.

[9] J.-F. Roussel et al., "SPIS open-source code: Methods, capabilities, achievements, and prospects," *IEEE Trans. Plasma Sci.*, vol. 36, no. 5, pp. 2360–2368, Oct. 2008.

[10] T. Muranaka et al., "Development of multi-utility spacecraft charging analysis tool (MUSCAT)," *IEEE Trans. Plasma Sci.*, vol. 36, no. 5, pp. 2336–2349, Oct. 2008.

[11] G. L. Delzanno, E. Camporeale, J. D. Moulton, J. E. Borovsky, E. A. MacDonald, and M. F. Thomsen, "CPIC: A curvilinear particle-in-cell code for plasma–material interaction studies," *IEEE Trans. Plasma Sci.*, vol. 41, no. 12, pp. 3577–3587, Dec. 2013.

[12] C. S. Meierbachtol, D. Svyatskiy, G. L. Delzanno, L. J. Vernon, and J. D. Moulton, "An electrostatic particle-in-cell code on multi-block structured meshes," *J. Comput. Phys.*, vol. 350, pp. 796–823, Dec. 2017.

[13] R. Marchand, "PTetra, a tool to simulate low orbit satellite–plasma interaction," *IEEE Trans. Plasma Sci.*, vol. 40, no. 2, pp. 217–229, Feb. 2012.

[14] G. L. Delzanno, J. E. Borovsky, M. G. Henderson, P. A. Resendiz Lira, V. Roytershteyn, and D. T. Welling, "The impact of cold electrons and cold ions in magnetospheric physics," *J. Atmos. Solar-Terr. Phys.*, vol. 220, Sep. 2021, Art. no. 105599.

[15] T. Nakagawa, T. Ishii, K. Tsuruda, H. Hayakawa, and T. Mukai, "Net current density of photoelectrons emitted from the surface of the GEO-TAIL spacecraft," *Earth, Planets Space*, vol. 52, no. 4, pp. 283–292, Apr. 2000.

[16] K. Kawasaki, S. Inoue, E. Ewang, K. Toyoda, and M. Cho, "Measurement of electron emission yield by electrons and photons for space aged material," in *Proc. 14th Spacecraft Charging Technol. Conf., (ESA/ESTEC)*, Noordwijk, The Netherlands, 2016, pp. 1–7.

[17] R. J. L. Grard, "Properties of the satellite photoelectron sheath derived from photoemission laboratory measurements," *J. Geophys. Res.*, vol. 78, no. 16, pp. 2885–2906, Jun. 1973.

[18] A. Pedersen et al., "Quasistatic electric field measurements with spherical double probes on the geos and isee satellites," *Space Sci. Rev.*, vol. 37, nos. 3–4, pp. 269–312, 1984.

[19] R. Schmidt and A. Pedersen, "Long-term behaviour of photo-electron emission from the electric field double probe sensors on GEOS-2," *Planet. Space Sci.*, vol. 35, no. 1, pp. 61–70, Jan. 1987.

[20] C. P. Escoubet, A. Pedersen, R. Schmidt, and P. A. Lindqvist, "Density in the magnetosphere inferred from ISEE 1 spacecraft potential," *J. Geophys. Res., Space Phys.*, vol. 102, no. A8, pp. 17595–17609, Aug. 1997.

[21] K. Ishisaka et al., "Electron temperature and density of magnetospheric plasma from GEOTAIL spacecraft potentials," *Adv. Space Res.*, vol. 24, no. 1, pp. 129–132, Jan. 1999.

[22] J. D. Scudder, X. Cao, and F. S. Mozer, "Photoemission current-spacecraft voltage relation: Key to routine, quantitative low-energy plasma measurements," *J. Geophys. Res., Space Phys.*, vol. 105, no. A9, pp. 21281–21294, Sep. 2000.

[23] B. Thiebault, A. Hilgers, A. Masson, C. P. Escoubet, and H. Laakso, "Simulation of the cluster-spacecraft floating probe potential," *IEEE Trans. Plasma Sci.*, vol. 34, no. 5, pp. 2078–2083, Oct. 2006.

[24] A. Pedersen et al., "Electron density estimations derived from spacecraft potential measurements on cluster in tenuous plasma regions," *J. Geophys. Res., Space Phys.*, vol. 113, no. A7, Jul. 2008, Art. no. A07S33.

[25] S. A. Boardsen, M. L. Adrian, R. Pfaff, and J. D. Menietti, "Inner magnetospheric electron temperature and spacecraft potential estimated from concurrent polar upper hybrid frequency and relative potential measurements," *J. Geophys. Res., Space Phys.*, vol. 119, no. 10, pp. 8046–8062, Oct. 2014.

[26] H. M. Mott-Smith and I. Langmuir, "The theory of collectors in gaseous discharges," *Phys. Rev.*, vol. 28, no. 4, pp. 727–763, Oct. 1926.

[27] G. L. Delzanno and X.-Z. Tang, "Charging and heat collection by a positively charged dust grain in a plasma," *Phys. Rev. Lett.*, vol. 113, no. 3, Jul. 2014, Art. no. 035002.

[28] V. A. Davis et al., "Surface-charging analysis of the radiation belt storm probe and magnetospheric MultiScale spacecraft," *IEEE Trans. Plasma Sci.*, vol. 40, no. 2, pp. 262–273, Feb. 2012.

[29] Y. X. Yuan, "A review of trust region algorithms for optimization," in *Proc. 4th Int. Congr. Ind. Appl. Math. (ICIAM)*, vol. 99. Edinburgh, U.K., 1999, pp. 271–282.

[30] P. A. Resendiz Lira, "Appendix: Synthetic cases," Zenodo, Los Alamos Nat. Lab. (LANL), 2022. [Online]. Available: https://www.zenodo.org, doi: 10.5281/zenodo.7072542.

[31] F. Pedregosa et al., "Scikit-learn: Machine learning in Python," *J. Mach. Learn. Res.*, vol. 12, pp. 2825–2830, Oct. 2012.

[32] C. Rasmusse and C. Williams, *Gaussian Processes for Machine Learning*. Cambridge, MA, USA: MIT Press, 2006.